Geophysical Journal International

Geophys. J. Int. (2014) **197,** 1627–1641
Advance Access publication 2014 April 4

doi: 10.1093/gji/ggu043

Scattering beneath Western Pacific subduction zones: evidence for oceanic crust in the mid-mantle

H. L. M. Bentham and S. Rost

School of Earth and Environment, University of Leeds, Leeds LS2 9JT*, UK. E-mail: h.bentham@see.leeds.ac.uk*

Accepted 2014 February 3. Received 2014 January 21; in original form 2013 August 15

SUMMARY

Small-scale heterogeneities in the mantle can give important insight into the dynamics and composition of the Earth's interior. Here, we analyse seismic energy found as precursors to *PP*, which is scattered off small-scale heterogeneities related to subduction zones in the upper and mid-mantle. We use data from shallow earthquakes (less than 100 km depth) in the epicentral distance range of 90°–110° and use array methods to study a 100 s window prior to the *PP* arrival. Our analysis focuses on energy arriving off the great circle path between source and receiver. We select coherent arrivals automatically, based on a semblance weighted beampower spectrum, maximizing the selection of weak amplitude arrivals. Assuming single *P*-to-*P* scattering and using the directivity information from array processing, we locate the scattering origin by ray tracing through a 1-D velocity model. Using data from the small-aperture Eielson Array (ILAR) in Alaska, we are able to image structure related to heterogeneities in western Pacific subduction zones. We find evidence for ∼300 small-scale heterogeneities in the region around the present-day Japan, Izu-Bonin, Mariana and West Philippine subduction zones. Most of the detected heterogeneities are located in the crust and upper mantle, but 6 per cent of scatterers are located deeper than 600 km. Scatterers in the transition zone correlate well with edges of fast features in tomographic images and subducted slab contours derived from slab seismicity. We locate deeper scatterers beneath the Izu-Bonin/Mariana subduction zones, which outline a steeply dipping pseudo-planar feature to 1480 km depth, and beneath the ancient (84–144 Ma) Indonesian subduction trench down to 1880 km depth. We image the remnants of subducted crustal material, likely the underside reflection of the subducted Moho. The presence of deep scatterers related to past and present subduction provides evidence that the subducted crust does descend into the lower mantle at least for these steeply dipping subduction zones. Applying the same technique to other source–receiver paths will increase our knowledge of the small-scale structure of the mantle and will provide further constraints on geodynamic models.

Key words: Mantle processes; Composition of the mantle; Subduction zone processes; Dynamics of lithosphere and mantle; Pacific Ocean.

1 INTRODUCTION

In the last few decades, seismic tomography has been very successful in imaging the large-scale structure of the interior of the Earth (e.g. Dziewonski & Woodhouse 1987; van der Hilst *et al.* 1991; Engdahl *et al.* 1995; Ritsema *et al.* 1999; Grand 2002; Huang & Zhao 2006; Ritsema *et al.* 2011). Dominant features in these studies are bands of fast seismic velocities that correlate well with the locations of past and current subduction zones and are interpreted as subducted oceanic plates or slabs in the Earth's mantle (van der Hilst & Seno 1993). Seismic tomography is not able to image the small-scale structure on the order of tens of kilometres related to chemical heterogeneities but these heterogeneities can give important information on large-scale flows, composition and evolution of the mantle.

Subducted slabs are the major driver to transport chemical heterogeneity through the upper mantle and sometimes into the lower mantle (Hofmann 1997; van Keken *et al.* 2002; Helffrich 2006; Rapp *et al.* 2008). Resolving the structure and dynamics of the compositional heterogeneity represented by these slabs is an important piece for our understanding of the chemical evolution of the mantle. Generally, the subducted slab consists of two large components: the harzburgitic lithospheric base and the basaltic upper crustal component, with a thin (∼1 km) layer of hydrous sediments deposited on the oceanic crust before subduction. Though some of the sediments might be transported into the mantle, most of the

sediments are likely to be removed during the subduction process (e.g. Patchett *et al.* 1984; Plank & Langmuir 1998) and are not important for the overall chemical heterogeneity of the subducted slab deeper in the mantle.

Recent studies of the short-period, scattered seismic wavefield have detected small-scale elastic heterogeneities beneath circum-Pacific subduction zones (Weber & Wicks 1996; Castle & Creager 1999; Kaneshima & Helffrich 1999; Krüger *et al.* 2001; Kito *et al.* 2008; Rost *et al.* 2008; Kaneshima 2009; Kaneshima & Helffrich 2009, 2010). These heterogeneities are commonly interpreted as the remnants of the subducted oceanic crust that are now located in the mid- and lower mantle. The elastic properties of these heterogeneities agree well with the expected properties of mid-oceanic ridge basalt (MORB) under high pressure and temperature (Rost *et al.* 2008) as determined by theoretical and experimental studies (Irifune & Tsuchiya 2007). The scale-length of the detected heterogeneities is typically on the order of 10 km, partly due to the dominantly 1 Hz seismic energy used in the analysis, but in good agreement with the typical thickness of subducted crust and the typical distance between normal faults at subduction zones (Ranero *et al.* 2003).

Most seismological studies imaging these heterogeneities use *P*-to-*P* or *P*-to-*S* scattered energy arriving in the *P* coda. They often use some form of simplified time migration of the *P*-coda energy to locate, and study the heterogeneities. Kaneshima (2009) and Kaneshima & Helffrich (2009) use semblance analysis of *S*-to-*P* scattering to detect heterogeneities in the uppermost lower mantle in close proximity to slabs beneath several Pacific subduction zones. They conclude that the seismic data reveal the early stages of a mechanical mixing process of the subducted MORB into the mantle and that the density of the subducted material does not prevent it from being entrained into the lower mantle, that is, the basaltic crust does not de-laminate from the harzburgitic slab and does not remain in the upper mantle. Similarly, Kito *et al.* (2008) migrated anomalous energy in the *P* coda and found deep scattering for depths of 800 to 1900 km in the vicinity of the Nazca slab. Rost *et al.* (2008) detect scatterers down to depths of about 1000 km mainly beneath the steeply dipping Mariana and Tonga/Fiji subduction zones. The locations of the scatterers detected by Rost *et al.* (2008) also agree well with fast velocities observed in tomographic images. They conclude that they likely detect the subducted palaeo-Moho in the lower mantle.

The seismological detection of subducted crust is important for our understanding of the chemical evolution of the lower mantle especially since several studies indicate that some lower-mantle structures such as large low-shear velocity provinces might contain ancient subducted MORB material (Christensen & Hofmann 1994; Tackley 2000; Deschamps *et al.* 2010). Further seismological studies targeting the very fine-scale structure of the mantle will allow us to estimate the material flux from the surface to the lower mantle due to the subduction process. The material flux will depend on the slab descent speed, the density contrast of the subducted material and the mantle viscosity (Quinteros *et al.* 2010). Therefore, the seismic imaging of the subducted oceanic crust will provide constraints on these properties that are essential for mantle convection modelling.

Here, we will present results of a novel approach exploiting a probe and a seismic array that have been rarely used in characterizing fine-scale mantle structure. We analyse energy arriving prior to *PP*, recorded at the small-aperture Eielson Array (ILAR) in Alaska. In particular, we are interested in energy that scattered off the great circle path (between source and receiver) and arrives as coherent precursors to *PP* (denoted *P***P*; Rost *et al.* 2008). We employ a weighted semblance analysis similar to Kaneshima (2009) and Kito *et al.* (2008). Our results indicate the existence of heterogeneities beneath the subduction zones of the Western Pacific. Using array directivity information, we locate heterogeneities with a low degree of lateral and vertical uncertainty to depths of 1880 km. We find that the locations of deep scatterers agree well with the location of the core of fast seismic anomalies found in tomographic studies interpreted as subducted slabs (e.g. Ritsema *et al.* 2011) and support previous results sampling the same region (Kaneshima & Helffrich 1999; Castle & Creager 1999; Rost *et al.* 2008; Kaneshima & Helffrich 2009, 2010), while giving new insight into the dynamics of slab transport in the mid-mantle.

2 DATA

We investigate seismic energy related to seismicity from Western Pacific subduction zones, recorded at the Eielson Array in Alaska (Fig. 1). ILAR is located approximately 90° to 110° away from several western Pacific subduction zones, a distance ideal for the study of scattered *PP* precursory energy (Rost *et al.* 2008). *PP* is a seismic phase that has reflected once midway between source and receiver (Fig. 2). *PP* and related energy have been used extensively for studying mantle structure (e.g. King *et al.* 1975; Kato & Hirahara 1991; Revenaugh & Jordan 1991; Estabrook & Kind 1996; Weber & Wicks 1996; Flanagan & Shearer 1998; Rost & Weber 2002; Deuss *et al.* 2006; Rost *et al.* 2008). This source–receiver configuration and the selected seismic time window will allow the study of several subduction zones including Japan, Izu-Bonin and the Marianas (Fig. 1a). ILAR is a small-aperture (10 km) seismic array and is designed to detect high-frequency signals from underground nuclear explosions (Fig. 1c), so is well suited to studying the high-frequency *PP* wavefield. ILAR consists of 19 short-period, vertical component seismometers quasi-randomly distributed over a circular area. A single three-component broad-band instrument (IL31) is located at the centre of the array (lat: 64.77, lon: −146.89) along with the short-period station IL01. The circular, quasi-random distribution of the seismic stations ensures little spatial aliasing and suppression of side-lobes in the array response function (ARF; Fig. 1b). Slowness wavenumber resolution of the array is not optimal due to the small aperture, but advanced array processing described in the next section will allow to precisely determine the directivity of the incoming seismic wavefield.

We process 239 earthquakes that occurred during 2000 to 2012 with magnitude (M_w) greater than 6 and within distances from 90° to 110° from ILAR, allowing us to sample Western Pacific subduction zones. Global stacks of teleseismic data between 90° and 110° show scattered energy arriving ∼100 s before *PP* (Rost *et al.* 2006). This time window is well suited to study the scattered energy because it is free from *P*-coda energy (Fig. 3), other main phases (e.g. PKiKP, PcP) and depth phases (and their codas) for shallow to intermediate depth earthquakes (Rost *et al.* 2008).

Data are bandpass filtered with corner frequencies of 0.5 and 1.4 Hz; the frequency band that has been found to be most appropriate for the targeted scattered energy (Fig. 4). We manually remove obvious data errors (e.g. spikes) and trends from the seismograms. We only select events with strong *PP* arrival to aid precise traveltime measurements and discard traces with a signal-to-noise ratio (SNR) of less than 4 [SNR calculated as *PP* amplitude relative to the noise prior to the P/P_{diff} arrival, i.e. the *P*-wave diffraction along the core mantle boundary (CMB)]. We only retain events with more than 10 traces after this selection for further analysis.

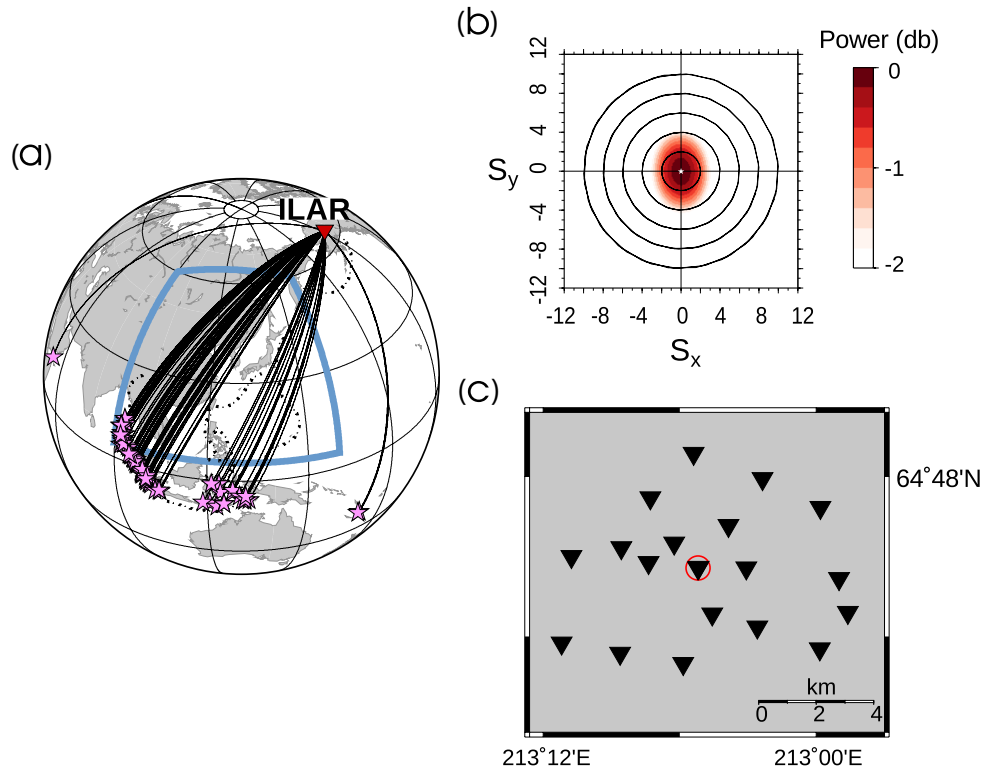

Figure 1. (a) The 95 earthquakes that contained scattering in this study (pink stars) are recorded at the Eielson Array (ILAR) in Alaska (red triangle) and travel along great circle paths (black solid lines) through Western Pacific subduction zones. Locations of ocean trenches (dotted black lines) are from the RUM model (Gudmundsson & Sambridge 1998). The study region (blue box) is bounded by latitude: 5°–60° and longitude: 90°–160°. (b) Array response function (horizontal slowness components, S_x and S_y) for the ILAR array. (c) ILAR array consists of 19 short period stations (black triangles) and one broad-band station (red circle) with coordinates (64.77°N, 146.89°W).

Due to the low energy of P_{diff} in the short-period recordings, we chose to use *PP* as the reference phase for the determination of the relative traveltime of the precursors. We use traveltimes calculated for the 1-D earth model ak135 (Kennett *et al.* 1995), as a reference and pick the *PP* arrival time from the data of the central broad-band station within ±50 s of this traveltime. We are aware that all 1-D earth models struggle to correctly predict *PP* traveltimes (Kennett *et al.* 1995), but tests show that ak135 shows the smallest error between picked and predicted traveltimes for *PP*. We account for local velocity variations as described in Section 4. *PP* is first identified in broad-band data since the additional passes of *PP* through the crust further attenuate the higher frequencies of *PP*; therefore, the phase is detected more easily at longer periods ($T > 5$ s). We include a second step of picking *PP* to avoid the strong Moho reflection (PmP) that dominates the short-period records (Fig. 4). Using the *PP* broad-band pick as a guide, we define a time window of ±4 s and select the best *PP* arrival as the highest amplitude arrival within the window, for each short-period station seismogram. Despite this careful picking procedure, there remains a *PP* traveltime uncertainty of 1 s, as the short-period *PP* waveform is complicated due to the interaction with the layered crust at the reflection point (Rost & Weber 2001). As expected, the picking error will add to the uncertainty in scatterer relocation (see Section 4).

The energy related to the *PP* scattered wavefield can be observed in individual seismic traces and in array beam traces (Figs 3 and 4). To maximize the detection of weak arrivals amongst the noise level, we use a selection tool based on the semblance and directivity properties of the *PP* precursors as described in the next section.

3 METHOD

We search for anomalous energy arriving prior to *PP* that is generated by scattering from small-scale heterogeneities in the mantle. We extract directivity information (slowness and backazimuth) from these arrivals to increase their SNR in order to extract the low-energy precursors from the noise and to locate of the origin of the scattered energy. We treat the process generating this energy as a scattering process, although reflections of an extended dipping interface probably contribute to the observed energy (Kaneshima 2009).

PP is a minimum–maximum traveltime phase with respect to variations along and perpendicular to the source–receiver plane and energy reflected from interfaces at depth arrives as *PP* precursors. Though previous studies have found *PP* precursors to be underside reflections off mantle discontinuities (e.g. Shearer 1990; Flanagan & Shearer 1998; Deuss *et al.* 2006) and asymmetric reflections (Wright 1972), these precursors arrive along the great circle path. We only consider precursors that arrive off great circle path (Fig. 2), like those found in Rost *et al.* (2008). The off great circle path reflected or scattered *PP* wavefield (*P*P*) is best observed in the distance range of 90°–110° (Wright 1972; Rost *et al.* 2006, 2008) and arrives in a time window up to 100 s before the *PP* arrival.

To avoid a bias of selecting higher amplitude scattered arrivals that are visually more prominent in the seismic data, we have developed an automatic approach (TOPCAT: toolkit for out-of-plane coherent arrivals tracking), which exploits waveform coherence to detect and extract information from the scattered energy. Explicitly, we use a semblance weighted beampower as a measure of

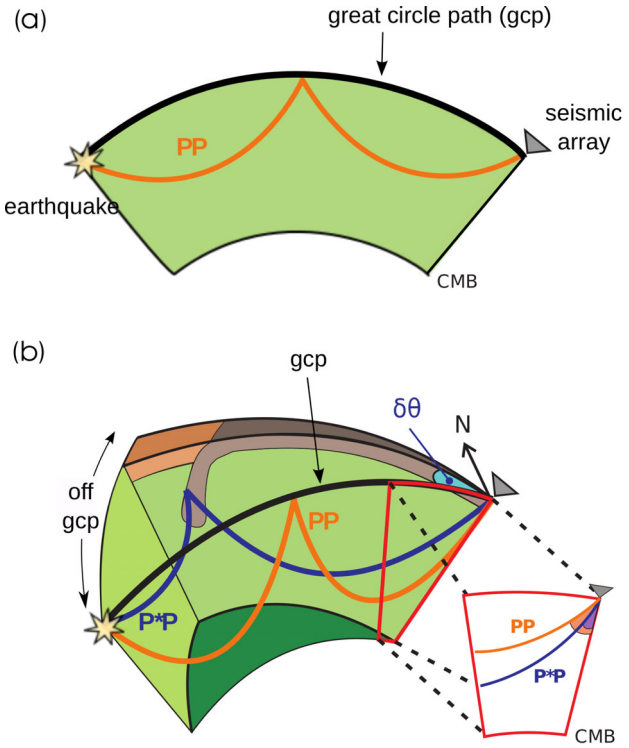

Figure 2. (a) *PP* (orange path) travels along great circle path (black line) between earthquake and array. (b) A precursory arrival to *PP*, denoted *P*P* (purple path) may arrive at the array due to scattered energy from a subducted slab that lies off the great circle path. The two arrivals have different backazimuths (difference in backazimuth labelled as $\delta\theta$) and different incident angles (shown in the insert). After Rost *et al.* (2008).

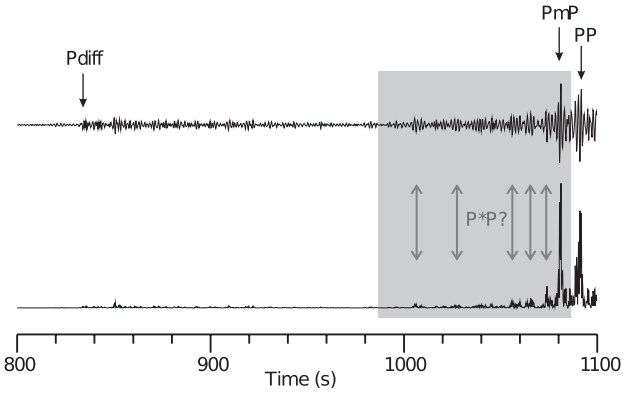

Figure 3. *PP* beamed seismogram (top) and *PP* beamed and squared seismogram (bottom) for earthquake on 2009 April 15, 20:01 (lat: −3.12, lon: 100.47, dep: 22 km, epicentral distance 102.33°, M_w: 6.3). Beam was formed from aligning traces from all 19 short period stations using theoretical *PP* slowness and backazimuth. Phases P_{diff} and *PP* are marked, as well as the 100 s window before *PP*, which contains weak energy that may be *P*P* arrivals.

the coherence and amplitude of the pre-*PP* energy. We calculate semblance (Neidell & Tanner 1971) of the signal, *f*, for *M* stations, through:

$$S_c = \frac{\sum_{j=k-\left(\frac{N}{2}\right)}^{k+\left(\frac{N}{2}\right)} \left\{ \sum_{i=1}^{M} f_{i,j(i)} \right\}^2}{M \sum_{j=k-\left(\frac{N}{2}\right)}^{k+\left(\frac{N}{2}\right)} \sum_{i=1}^{M} f_{i,j(i)}^2}, \quad (1)$$

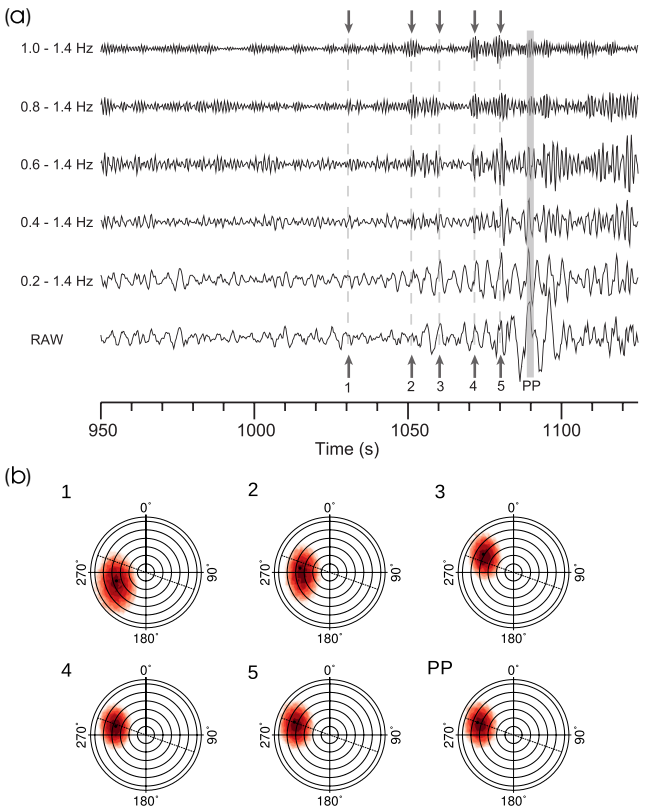

Figure 4. (a) *PP* beam data from earthquake on 2009 April 15, 20:01 (see Fig. 3) for different frequency bands. Data were filtered with five different bandpass filters. Observed *PP* arrives at 1090 s and is identified until the 0.8–1.4 Hz band (*PP* highlighted in grey). At least five coherent arrivals as precursors to *PP* are notable in most frequency bands. Precursors are marked by the arrows and dashed lines. (b) Polar plots showing the optimum slowness (radial axis) and backazimuth (angular axis) found using fk analysis for precursors marked 1–5 and for the *PP* arrival. Dashed line marks the backazimuth for the great circle path. Radial circles mark every 2 s/° of slowness (see Fig. 1b for power scale).

where *N* is the number of samples in the time window and *k* indicates the sample at the centre of the semblance time window. We apply a sliding-window approach (Rost & Weber 2002) to calculate semblance in a short (3 s) time window, shifting it across the 100 s precursory window before *PP* energy, stepping by 0.2 s between windows. A time window of 3 s allows the inclusion of the dominant period of the scattered energy and overlapping windows allow centring of the energy limiting any truncation of the waveforms. The slowness vector (slowness and backazimuth) in each time window is determined using frequency-wavenumber (fk) analysis (Capon 1969). We use the slowness and backazimuth to correct for moveout of the signal in each analysis window, and sum the traces from each station to produce a beamtrace and measure its amplitude (*A*). The semblance coefficient S_c for each time window is used to weight the beampower by $S_c^2 \times A$. We create a normalized semblance weighted beampower (NSWB) time-series by dividing the spectrum by the weighted beampower of *PP*. The variations in slowness, backazimuth, semblance, beampower and NSWB across the 100 s time window of an example event are shown in Fig. 5. We define a precursor as energy arriving with a NSWB >0.1, a threshold that has been found in resolution studies to give the best detection rate for typical noise levels (a technical description of this testing can be found in the Supporting Information, Fig. S1).

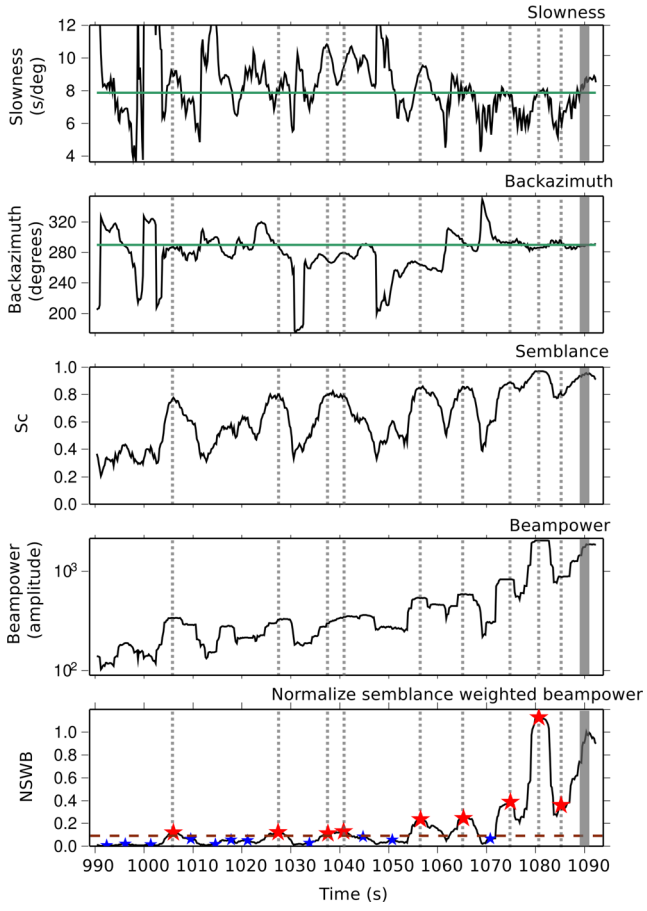

Figure 5. An example of the results from TOPCAT for event 2009 April 15, 20:01 (see Fig. 3). From top to bottom: plots show variations in time of slowness, backazimuth, semblance coefficient, Beampower and normalized semblance weighted beampower (NSWB). Theoretical *PP* slowness (7.515 s/°) and backazimuth (289.38°) marked by green horizontal lines. Peaks in the NSWB spectrum that are below the 0.1 threshold are marked with blue stars and those above the 0.1 threshold and classified as precursors are marked with red stars and grey dashed lines.

Additionally, a precursor must be at least 3 s from another selected precursor to avoid multiple detection of a precursor in the analysis window. We define a scattered arrival as a precursor with a backazimuth that is greater than ±5° from the observed *PP* backazimuth to avoid in-plane underside reflections.

Scatterer traveltime is selected as the time of the maximum beampower within the analysis window. For a scattered precursor detection, we use the measured traveltime, backazimuth and corrected slowness (for discussion, see Section 4) to locate the scatterer origin using ray tracing through the 1-D earth model ak135 (Kennett *et al.* 1995). Slowness and backazimuth define a ray from receiver to scatterer origin. We use the scatterer traveltime relative to *PP* to locate the exact location (in latitude, longitude and depth) along this ray by minimizing the misfit between measured traveltime and theoretical traveltime with a vertical grid spacing of 20 km. Scatterers with traveltime misfit of more than 1 s are discarded from the analysis. Tests with the data show that only *P*-to-*P* scattering gives reasonable results in the relocation and we are not able to find solutions for *S*-to-*P* or *P*-to-*S* scattering. Therefore, we assume that we only observe *P*-to-*P* scattered energy on the vertical instruments at ILAR.

4 CORRECTIONS AND ERRORS

We observe differences between the *PP* slowness and backazimuth as measured at the array and the *PP* slowness and backazimuth derived from 1-D reference models for the same source–receiver geometry. Therefore, for a precise localization of the scattering heterogeneity, a slowness correction is necessary to account for local receiver structure influencing the slowness vector measurements. We cannot apply published corrections for ILAR (Lindquist *et al.* 2007) for this data set due to the differences in distance (i.e. slowness) and backazimuth ranges used. Instead, we derive slowness/backazimuth deviations from the data by collating slowness and backazimuth measured for *PP* for each event compared to the theoretical values for ak135. The measured uncertainties are displayed as mislocation vectors between expected and measured slowness and backazimuth values (see Fig. S2). We find that the mean of the observed slowness is less than the mean of the calculated slowness, with a difference of 0.46 s/°. Since the average observed slowness is less than the theoretical values, the *PP* waves are arriving steeper than expected, which could be caused by the higher velocity layer of the Aleutian subducted slab (Lindquist *et al.* 2007). As we observe little variation of slowness deviation with distance or backazimuth, we apply a bulk shift of 0.46 s/° to the *PP* precursors to correct for 3-D structural variations beneath the array. The difference in the means of the observed and theoretical backazimuth is small ($\Delta\theta \approx 0.83°$) but differences between observed and theoretic backazimuth vary greatly with backazimuth. The lack of azimuthal coverage in our data set limits a comprehensive analysis of azimuthal correction, and therefore we do not attempt to correct for backazimuth deviations (see Fig. S2).

Several errors will contribute to the mislocation of the scatterer origin as determined in our approach. These are either related to the array measurement or the uncertainty in ray tracing through a 1-D earth model as used in the relocation approach. We can estimate uncertainties in determining slowness, backazimuth and traveltime at the array and use these to derive errors in latitude, longitude and depth of the scatterer locations. The slowness/backazimuth measurements with the fk-analysis depend on the noise conditions in the time window. Therefore, the comparison with the major phase *PP* alone might underestimate the error attached to the measurement. Using simple synthetic time-series, simulating arrivals for varying slowness and backazimuth, we aim to estimate the accuracy of the slowness, backazimuth and traveltime measurements. We vary signal energy relative to noise level and use pre-signal noise recorded at ILAR for these tests. The synthetic data are processed identically to recorded data and the resultant parameters are compared to the input parameters to extract realistic error estimates (Table 1). We conclude that for good data noise levels (SNR *PP*/precursor >4), the accuracy of the measurements for slowness, backazimuth and traveltime are ±0.19 s/°, ±1.2° and ±0.5 s, respectively. The precision of traveltime determination is important since it would

Table 1. Input directivity and traveltimes for *PP* and 1 precursor, and output slowness (u), backazimuth (θ) and traveltime relative to *PP* (δt) from TOPCAT.

	u (s/°)	θ (°)	δt (s)
PP (input)	7.5	285	–
PP (TOPCAT result)	7.51	285.7	–
Precursor (input)	7.0	270	6.0
Precursors (TOPCAT result)	7.19	268.8	5.5
Detection errors	0.19	1.2	0.5

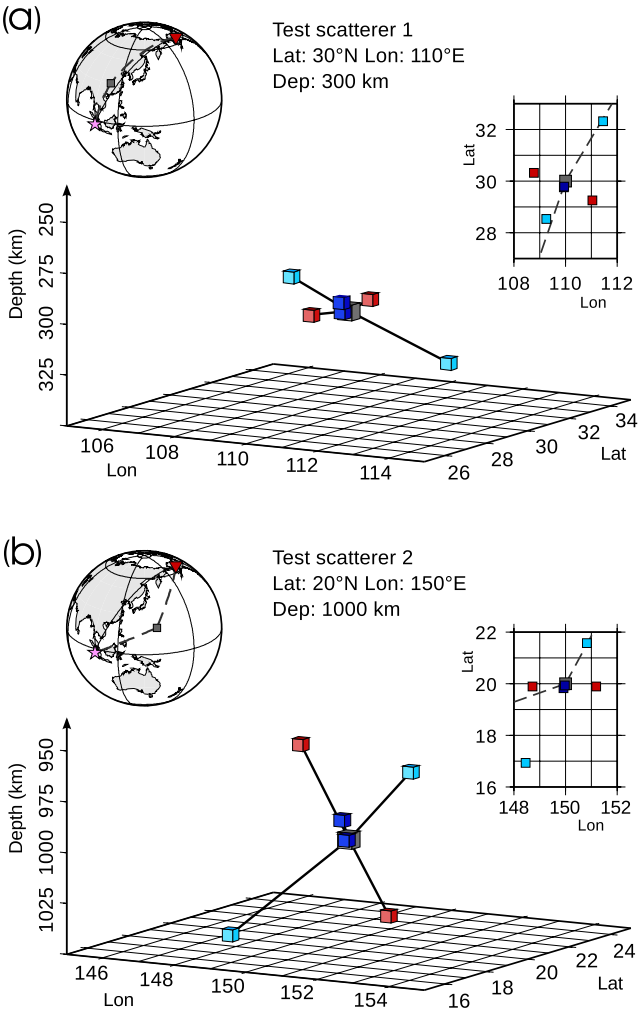

Figure 6. Relocation errors for two test scatterers each with six relocation cases for (a) shallow scatterer at: 30°N, lon: 110°E and dep: 300 km and (b) deep scatterer at: 20°N, lon: 150°E and dep: 1000 km. Grey cubes—true location of scatterer; red cubes—scatterer location with slowness errors; blue cubes—scatterer location with backazimuth errors; cyan cubes—scatterer locations with traveltime errors.

add large uncertainties in scatterer locations. We avoid problems with cycle skipping by not allowing a *P*P* detection within 3 s of another. Since we use a NSWB with a grace period of 3 s after a detection (i.e. there are at least 3 s between precursor detections) and most of the precursor waveforms have a duration of ∼1 s, the whole wavelet is included in the analysis time window.

Using these detection uncertainties in the backprojection procedure, we find that the smallest errors for latitude, longitude and depth are generated with the errors in traveltime (0.2°, 0.6° and 5 km, respectively), whereas the largest errors are due to errors in slowness (3°, 1.5° and 40 km). Errors in depth are slightly greater for a scatterer at $h = 1000$ km, but errors in coordinates do not greatly increase with depth. Results are shown in Fig. 6 (see Table S1 for results).

We calculate the potential error due to 3-D velocity variations in contrast to the 1-D approach followed here by ray tracing along scatterer paths through a 3-D tomographic model (Widiyantoro *et al.* 1999). We find an average error of ±0.5 s (Fig. S3), which is similar to the traveltime picking error and translates to an additional ∼50 and 5 km of mislocation in the laterally and in depth, respectively. In summary, we find that our locations are accurate to ±300 km laterally and 65 km for realistic slowness, backazimuth and traveltime errors, giving us a very good localization of heterogeneities using this method.

5 RESULTS

We find 282 off-azimuth precursors from 95 events with detectable energy in the NSWB time-series (Fig. 7). An additional 137 precursors arrive along great circle path (±5°) and likely represent underside reflections. For the off-azimuth precursors, 34 per cent are found in the shallow subsurface (0–100 km), 53 per cent occur in the uppermost mantle (100–400 km), 7 per cent occur in the transition zone (400–600 km) and 6 per cent are found in the mid- and lower mantle (deeper than 600 km). We observe a decrease in the number of scatterers with depth (Fig. 8), which is not related to the detection capability of the method (see Section 6 for more details). We find that there are a couple of instances where we image the same scatterer (i.e. identical locations within the error bounds), and this provides confidence into our results. However, the scarcity of these detections prevents any further interpretation.

Additionally, we observe a general decrease in amplitude strength of NSWB with depth. However, detections deeper than the transition zone show constant but weak amplitude in NSWB (NSWB less than 0.3). As the precursors are weak and generally below the noise level of individual traces, it is difficult to study the waveforms of the precursors. However, we do observe that many of the precursor beams have a spindle-shape form for high frequencies, similar to the spindle-shape of *PP* (Fig. 4). Unfortunately, the low amplitude of the precursors prevents any further analysis of the waveform of the scattered energy.

Fig. 9 shows detected scatterer locations at depths from 300 to 600 km in 100 km intervals. The scatterer locations in these four depth intervals correlate well with slab contours from the RUM

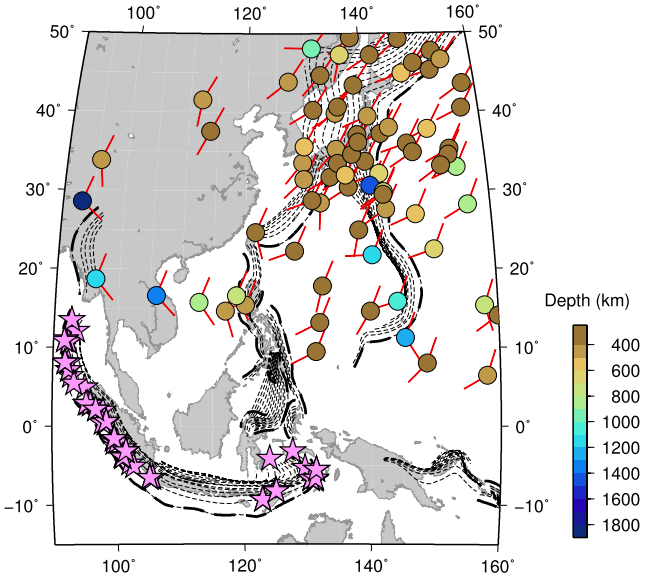

Figure 7. Locations of scatterers in the Western Pacific (range from 250 to 1900 km; shallow to deep are brown to blue, respectively) collated with the angles of approach and scattering of the *P*-to-*P* precursor (red vectors). Ocean trenches zones are shown in thick dashed blacked lines. RUM model subduction zone contours (Gudmundsson & Sambridge 1998) are shown as thin black dashed lines (contour interval of 50 km). Events studied and contain evidence of scattering are shown as pink stars.

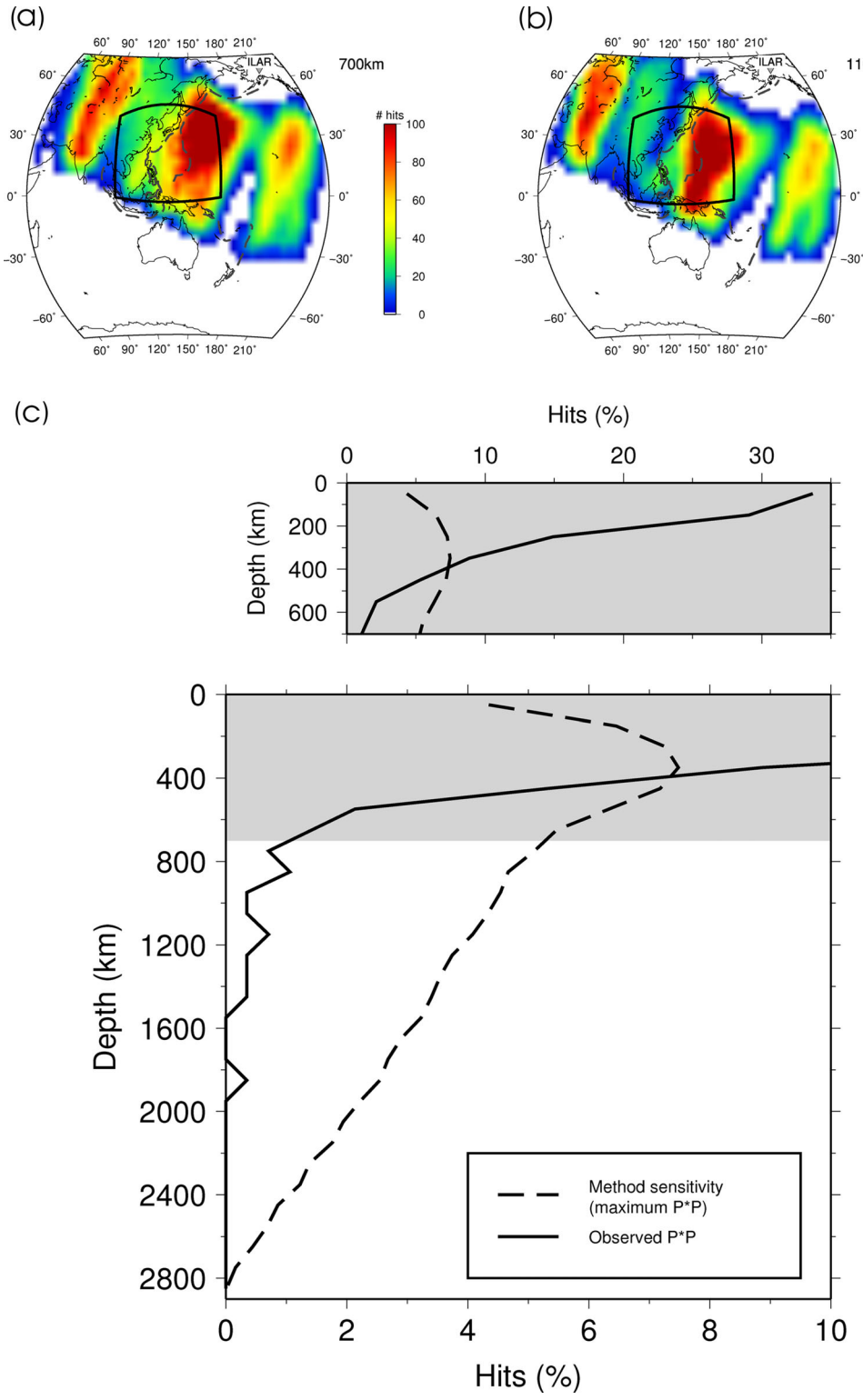

Figure 8. Sensitivity analysis of the *PP* scattering probe. For each source–receiver combination for all 239 earthquakes in the data set, the sensitivity of *PP* precursor scattering detection method is found by creating a grid in longitude and latitude (for every 20 km in depth) and for each cell, we evaluate if it is possible for a precursor to be generated with backazimuth that fall within ranges derived from precursors found in the data (e.g. $-60^\circ \geq \theta \leq 60^\circ$); and with slowness (e.g. $u \geq 4.5$ s/°, for $\Delta \leq 95^\circ$) and traveltime (e.g. 3 s $\geq t \leq$ 100 s before PP) limits that are suitable for the method applied. By combining all the contributions from each event for each cell, we obtain the total sensitivity for every cell for each depth slice and such sensitivity maps are shown for depths 700 (a) and 1100 km (b) (most sampled regions are in red and regions with no detectability in white). The study region for this data set is bounded by the black box, and position of ocean trenches is shown in dark grey dashed line. (c) Graph showing the number of observed precursors (at each depth) as a percentage [or Hits (per cent)] of the total observed precursors (solid black lines). In addition, the number of scatterers that could be detected at each depth (based on source–receiver geometry, velocity model and relocation method used, that is, the method sensitivity), is shown as a percentage of the total precursors that can be found in the study region (dashed black lines). Insert: upper mantle and transition zone scatterers in more detail.

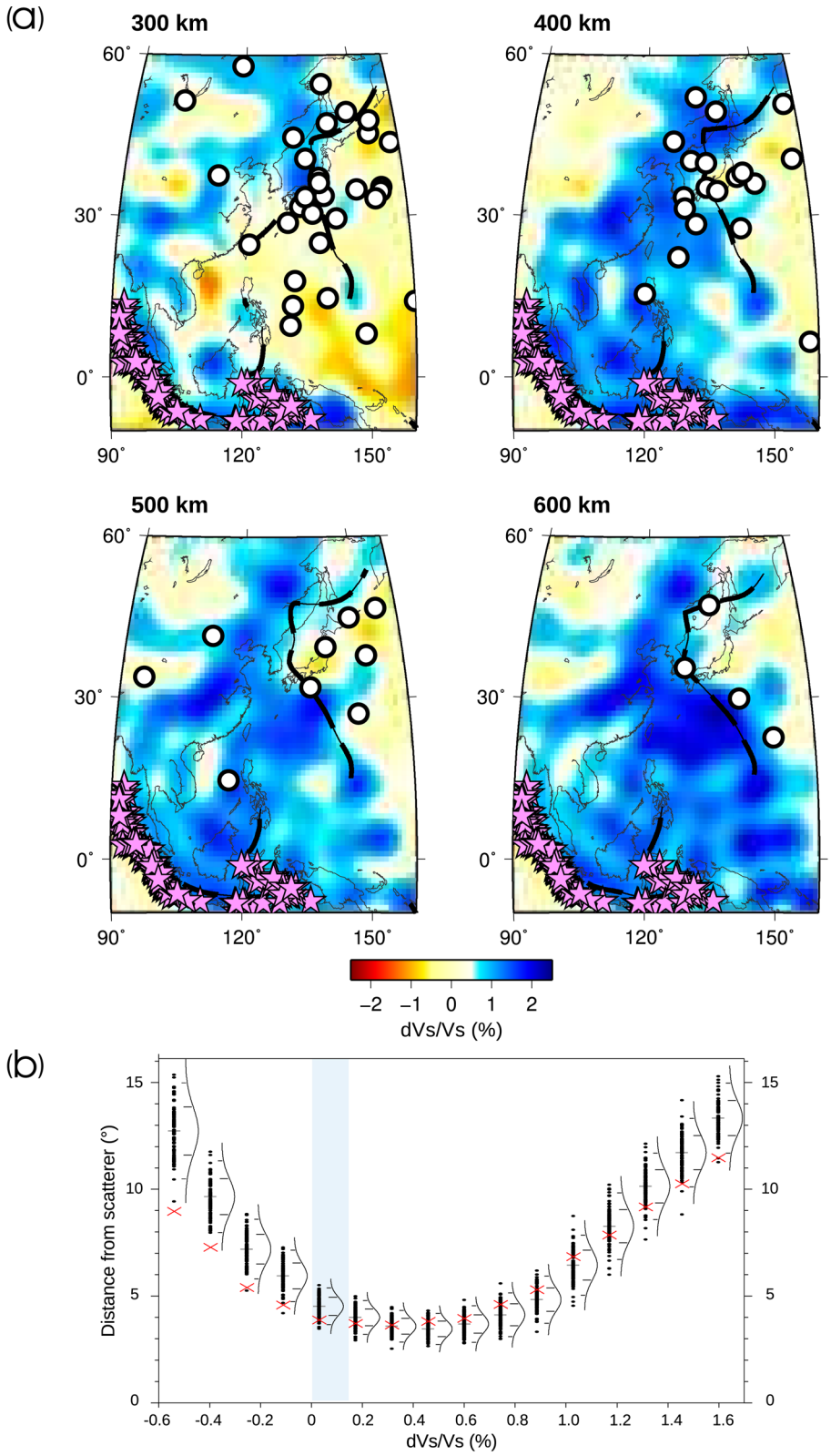

Figure 9. (a) Depth slices for 300–600 km (100 km interval) of S40RTS tomography model (Ritsema *et al.* 2011), scatterer locations in intervals defined as ±50 km of each depth (black circles), RUM model subduction contours (dashed black lines; Gudmundsson & Sambridge 1998) and locations of earthquakes that show scattering (pink stars). (b) Method of quantitatively assessing the correlation between scatterer locations and S40RTS tomography model. The mean distance between the scatterer locations and intervals of velocity variation are evaluated (red crosses). In addition, the mean distance between 100 random data set of scatterer locations and intervals of velocity variation are calculated (black dots), and are used to generate the mean (grey horizontal lines), standard deviation 1σ (inner black lines on Gaussian curves) and 2σ (outer black lines on Gaussian curves). The best correlation is chosen for the velocity variation interval of 0–0.17 per cent (blue box) as this interval has the lowest mean distance and lies outside at least 1σ.

model (Gudmundsson & Sambridge 1998) and clusters of scatterers are correlated with the triple junction between the Marianas, Japan and Western Philippine slabs. The comparison of scatterer locations with tomographic images (Ritsema *et al.* 2011) shows a good correlation of scatterer location with the edges of fast anomalies (Fig. 9a); in particular, scatterers correlate with velocity variations of −0.5 to 0.5 per cent.

We can determine the best correlation of scatterer locations with structures in the S40RTS tomographic models by calculating the distances between scatterers and intervals of velocity variation ($\mathrm{d}V_s/V_s$). The mean distances between the scatterers and intervals of $\mathrm{d}V_s/V_s$ (denoted as $\delta\bar{d}$) are evaluated to establish if there is a range of values that are preferentially closer to the scatterer locations (Fig. 9b). Comparing $\delta\bar{d}$ to the mean distances calculated for 100 random scatterer data sets (with the same number of scatterers and depth distribution statistics) and establishing the mean and standard deviation (σ) of the random data sets, the preferred $\mathrm{d}V_s/V_s$ range is 0–0.17 per cent. This range lies outside 1σ, demonstrating that there is 66 per cent confidence that the correlation has not occurred by chance.

We calculate the tomography gradient of S40RTS for depth slices 300–600 km (Fig. 10a) as the gradient of tomographic velocity structures has been useful in the interpretation of smaller scale structure (Thorne *et al.* 2004). The contours of low gradients (<0.30 per cent/°) correlate with the edge of the fast velocity features in S40RTS and are likely to be the edge of the slab. In addition, scatterers show good visual correlations with the tomography gradient of 0.14–0.23 per cent/° (Fig. 10a). Producing mean distance calculations for the tomography gradient (Fig. 10b), the preferred gradient ranges are 0.14–0.19 and 0.19–0.23 per cent/°, which lie outside 1σ and 2σ, respectively. While the range 0.14–0.19 per cent/° has the lowest $\delta\bar{d}$ (1.33°), the $\delta\bar{d}$ for 0.19–0.23 per cent/° is close to this minimum (1.51°) and this latter range shows a better correlation of 2σ, equating to 95 per cent confidence that the correlation has not occurred by chance. Therefore, it is likely that the gradient that best represents the scatterer locations is within the range 0.14–0.23 per cent/°.

In contrast, the relocated scattered energy shows a poor correlation with the largest gradients of 0.40–0.76 per cent/°, which at some depths corresponds to the core of the slab (e.g. for depths 500 and 600 km). Therefore, in agreement with previous studies (e.g. Rost *et al.* 2008; Kito *et al.* 2008), we likely observe scattering from the top or bottom of the subducted crust. However, considering scattering angles and subduction contours as well (Fig. 7), we suggest that the energy we detect is probably from underside reflections (Kito *et al.* 2008) and not reflections from top of the slab.

We find 17 scatterers deeper than 600 km (from here on referred to as deep scatterers). We expect a reduction of scatterer detection at this depth as shown in the sensitivity analysis (see Fig. 8 and Section 6). Deep scatterers are located north of the Indonesian slab; underneath the current position of the Mariana/Izu-Bonin trenches; and to the east of the Mariana/Izu-Bonin trenches. The deepest scatterer found in this study (at 1880 km deep) is located in the first region, ∼200 km northeast of the Assam subduction zone (Fig. 11). Four other scatterers in this area are located at depths of 790–1385 km. Each of these scatterers is generated off great circle path by more than 20° but found in seismograms from different earthquakes. The scatterers form an arc tracing the present-day shape of the Sunda arc subduction system (Indonesia) offset northward by ∼15°. These scatterers correspond to a region of known lithospheric graveyards (Engebretson *et al.* 1992) and particularly coincide with the location of the Indonesian trench ∼100 Ma ago (e.g. Richards & Engebretson 1992; Wen & Anderson 1995; Hall 2012). Fig. 11(b) shows the location of these scatterers in side view (azimuth of sight is 341°). Using a tetrahedral interpolation of the scatterer locations in this subregion, we find that the scatterers do not outline a planar shape as would be expected from an unaltered subducted slab.

The second region (Mariana/Izu-Bonin subduction zones) contains eight scatterers ranging in depth from 600 to 1480 km and these correlate well with the position of the Marianas trench over the last 17 Myr (Seno & Maruyama 1984), as shown in Fig. 11(a). The tetrahedral interpolation of these scatterer locations shows an almost planar feature with a strike of ∼330° (Fig. 11b). This result agrees well with a dipping reflector found down to depths of ∼1600 km by Castle & Creager (1999, Fig. 11). Several other studies have also imaged scatterers in this region in the mid-mantle (Krüger *et al.* 2001) and to deeper depths in the mantle (∼1900 km, e.g. Kaneshima & Helffrich 1999, 2009, 2010) and are in good agreement with our results.

The remaining four deep scatterers are found between 730 and 885 km depth and lie more than 7° to the east of the most easterly position of the past Izu-Bonin and Mariana trenches, which is larger than the maximum error associated with locating scatterers in this study (recall errors of 3° and 1.5° for latitude and longitude, respectively). Other scatterers have been found in the region previously by Rost *et al.* (2008), especially beneath the Philippine Sea down to depths of ∼1000 km. We do not find scattering beneath the Philippine Sea in this study as the method is sensitive to other parts of the Western Pacific subduction region (due to the different source–receiver combinations) but agree with Rost *et al.* (2008) on scattering from a region east of Izu-Bonin. We are cautious to not overinterpret the few scattering points we have from these depths and therefore do not attempt to come to a conclusion on the structure underlying the heterogeneities at this stage.

6 DISCUSSION

This study gives further evidence for the existence of small-scale mantle heterogeneities that might be related to the subduction process. We analyse data with a dominant period of about 1 s, indicating that the heterogeneities leading to scattered energy are on the order of about 10 km. The high thermal diffusivity of mantle materials would allow thermal anomalies to dissipate within a few million years (van Keken *et al.* 2002), and therefore it seems likely that the scattered energy is generated from chemical heterogeneities. Although we treat the energy as being produced by scattering from small-scale heterogeneities, the detected energy might be related to dipping, sharp reflectors in the mantle (Castle & Creager 1999). An obvious candidate for this reflector is the subducted palaeo-Moho (Rost *et al.* 2008). Therefore, we relate the scattered energy to the subduction process since the study region is heavily influenced by past and present subduction.

From tomographic models (Widiyantoro *et al.* 1999; Grand 2002; Huang & Zhao 2006; Ritsema *et al.* 2011) and studies of the seismicity of subduction zones in the Western Pacific, it has been shown that subducted slabs in this region are roughly planar and continuous in the upper mantle to the base of the transition zone. Depth slices through the tomography model S40RTS (Ritsema *et al.* 2011) in the study region for depths 300–600 km (Fig. 9a) show that scatterer locations have some correlation with the edges of fast velocity features at these depths (Fig. 9b) and support the suggestion that the scatterers are reflected/scattered energy off the edge of the slab. Such a correlation does not extend past 600 km depth (scatterer

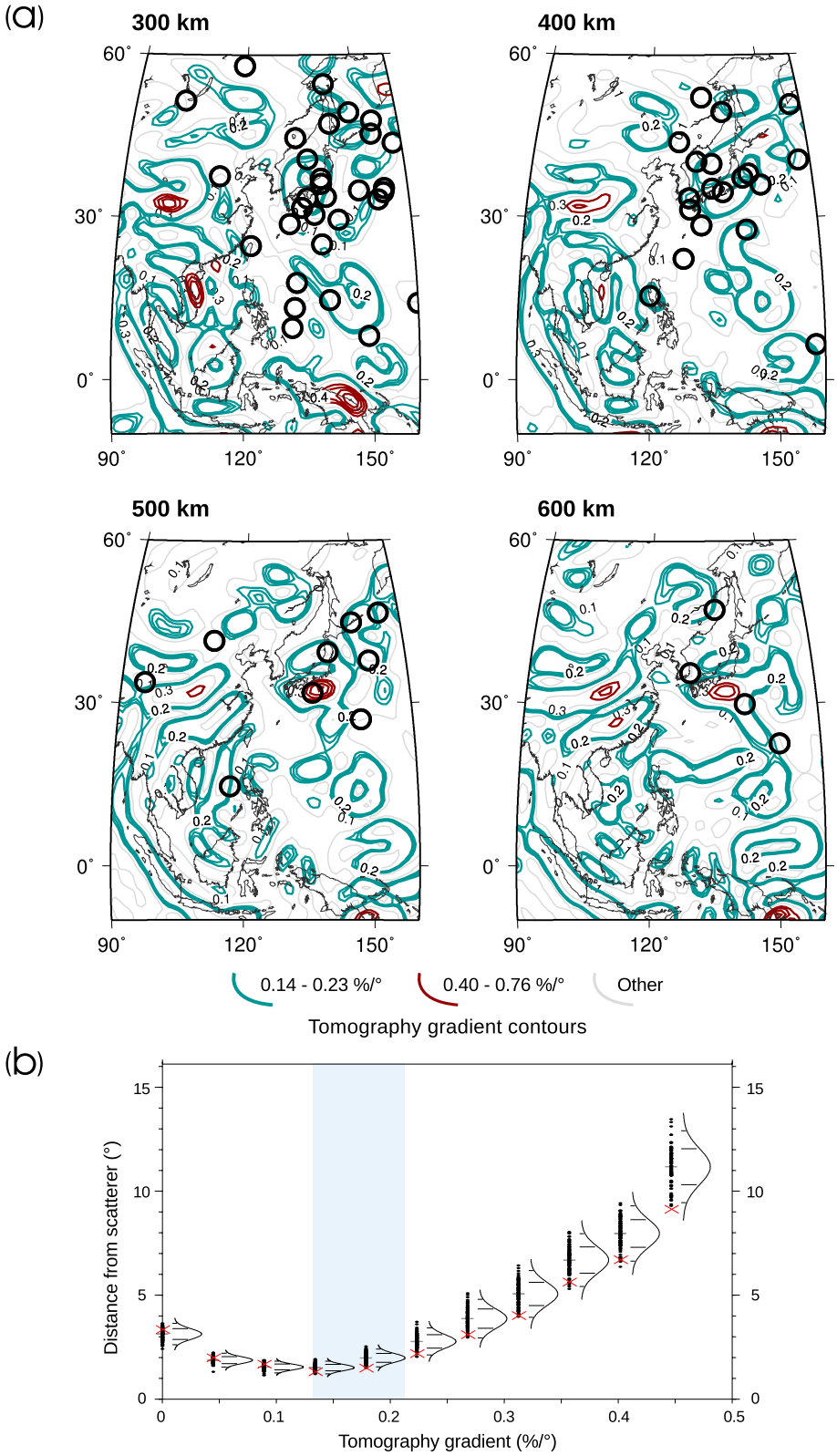

Figure 10. (a) Depth slices for 300–600 km (100 km interval) showing the gradient of S40RTS tomography model and scatterer locations in intervals defined as ±50 km of each depth (black circles). (b) Method of quantitatively assessing the correlation between scatterer locations and the gradient of the S40RTS tomography model. The mean distance between the scatterer locations and intervals of gradient are evaluated (red crosses). In addition, the mean distance between 100 random data set of scatterer locations and intervals of gradient are calculated (black dots), and are used to generate the mean (grey horizontal lines), standard deviation 1σ (inner black lines on Gaussian curves) and 2σ (outer black lines on Gaussian curves). The best correlations are chosen for the gradient intervals of 0.14–0.23 per cent/° (blue box) as these intervals generally have the lowest mean distances and lie outside at least 1σ.

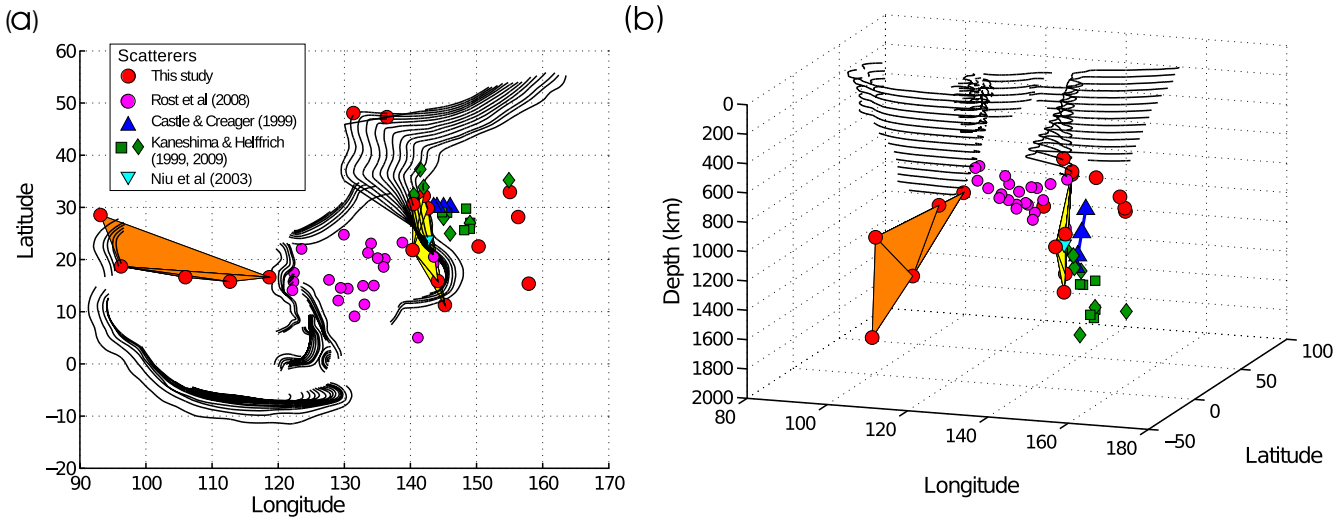

Figure 11. (a) Map and (b) side view with azimuth 341°, of the location of the 17 deep scatterers found in this study and scatterers found in previous studies (see legend). Tetrahedral objects are created for the scatterers beneath SE Asia (orange) and beneath the Izu-Bonin and Mariana trenches (yellow). Contours of the slab topography (solid black lines) are from the RUM model (Gudmundsson & Sambridge 1998) are shown for 50 km intervals in depth.

depths 550–650 km), although a clear correlation is difficult to make due to the reduction in the number of scatterers in the mid- and lower mantle.

We also find that the locations of shallow and transition zone scatterers show a correlation with the 0.14–0.23 per cent/° gradient of S40RTS (Fig. 10a). While one might expect the largest tomography gradient to coincide with the strongest compositional gradient, this is not observed here because the long-period nature of the tomographic image is likely more sensitive to the broader thermal signal of the slab. The scatterers located in this study are correlated with the smaller tomography gradients (Fig. 10b) corresponding to the edge of fast velocity features in the tomography model. The highest S40RTS gradients of about 0.76 per cent/° are observed in the centre of slabs (Fig. 10a) where compositional gradients are small and where previous studies have shown that thermal gradients are strong due to an insulated cold core of the slab (e.g. Helffrich *et al.* 1989; Davies & Richards 1992). As tomography is sensitive to long-wavelength structures, it may well be dominated by the temperature signature and only partly influenced by the compositional short-wavelength features.

Additional information on slab structure can be extracted from slab reconstructions such as RUM (Gudmundsson & Sambridge 1998) or Slab 1.0 (Hayes *et al.* 2012, Fig. S4), which show that the southern Izu-Bonin slab and the Mariana slabs are steeply dipping down to 700 km depth (Fig. 11). The slab reconstructions agree well with regional tomographic models which indicate fast seismic velocities continuing into the lower mantle (e.g. Huang & Zhao 2006). Both of the slab models show that there is a gradual change in dip angle of the northern part of the Izu-Bonin slab, north of latitude 33°. The Slab 1.0 model shows a gap in the slab beneath a slab tear at ∼35°N, 350 km depth, as highlighted in regional tomography (Obayashi *et al.* 2009), and is important in explaining the differences in subduction dip angle between the connected Japan and Izu-Bonin slabs. Deeper into the mantle (below 600 km) where slab models are absent and tomographic models are less well constrained (Fig. 12), interpretation of the scatterer distribution is not straightforward. Scatterers beneath the Izu-Bonin and Mariana subduction zones align to form a pseudo-planar shape oriented ∼330°, subparallel to the general profile of this subduction system in the present day (Fig. 11) and for the location of the palaeo-Izu-Bonin/Mariana subduction trenches up to 17 Ma (Seno & Maruyama 1984, Fig. 12a). Such a feature suggests that the steeply dipping Mariana slab is continuous and penetrates into the lower mantle, to depths of at least ∼1450 km, and contains a detectable crustal component. The inferred slab location in this study is consistent with previous observations of a dipping feature in the lower mantle (Castle & Creager 1999) and is in close proximity to other scatterers at a similar depth (Kaneshima & Helffrich 1999; Niu *et al.* 2003; Kaneshima & Helffrich 2009, 2010).

The Pacific Plate started to subduct under the Philippine Sea at least 43 Ma ago (Seno & Maruyama 1984) generating the Izu-Bonin/Mariana subduction zones and tomography shows that these slabs are steeply dipping (Huang & Zhao 2006; Ritsema *et al.* 2011). Though the subduction angle and style has probably changed during the lifetime of these subduction zones (Seno & Maruyama 1984; Miller *et al.* 2006), we can make a first-order calculation of how deep we can expect the slabs to have penetrated into the mantle, and thus if it is plausible that the scatterers we detect could be connected to the present-day subduction system. Assuming steeply dipping slab (constant subduction angle of 90°), subduction rate of 4.84 cm yr^{-1} as an average from rates over the last 0–8 Ma (Miller *et al.* 2006) and continuous subduction for the past 43 Ma, the Mariana slab could be present at depths of 2081 km. The deepest scattering associated with this slab has been observed in previous work at depths of 1900 km (Kaneshima & Helffrich 2009), consistent with the above calculation. Overall, this suggests that the Mariana slab, steeply subducting without any inhibitors to flow, likely reaches the lower mantle but not the lowermost mantle or the CMB, explaining the absence of scatterers in this region at these depths.

Though the Mariana slab is steeply dipping in the present day and is connected to an advancing trench at the surface, it has been documented that in the past, the slab was stagnant and horizontal at the base of the transition zone while experiencing a period of trench retreat (Seno & Maruyama 1984; Miller *et al.* 2006). Trench retreat would have caused the trench to move eastwards and after the trench switches to migrating westwards, the slab may have penetrated into the lower mantle and anchored (Seno & Maruyama 1984; van der Hilst & Seno 1993; Miller *et al.* 2006) resulting in strain within the

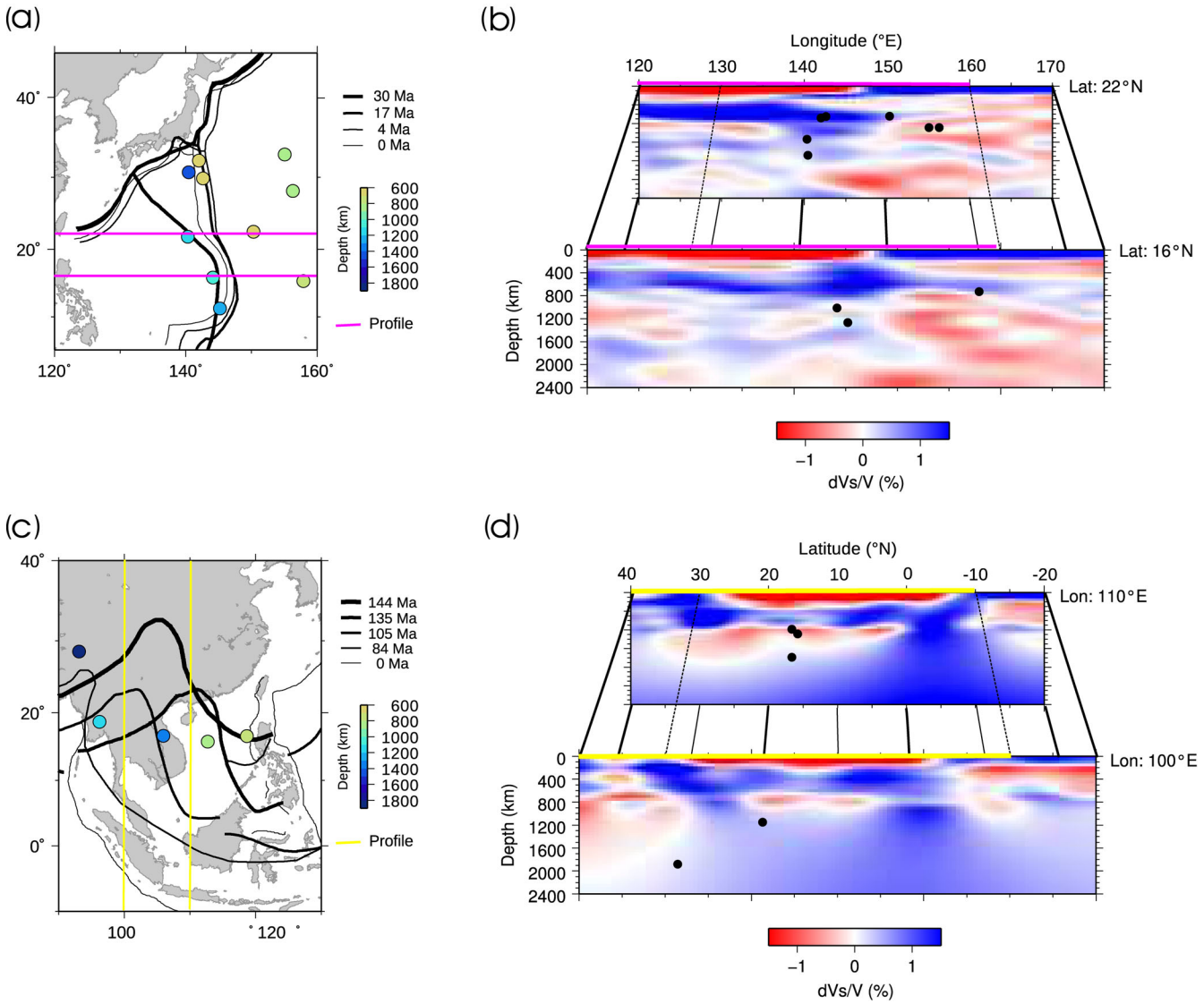

Figure 12. (a) Location of deep scatterers (circles, coloured by depth) in Izu-Bonin/Mariana subduction region with location of ancient subduction trenches (Seno & Maruyama 1984) where thickness of line represents year. (b) Two E–W cross-sections through S40RTS (Ritsema *et al.* 2011) tomography model in the Izu-Bonin and Mariana subduction region with location of scatterers (black circles). (c) As (a) but location deep scatterers (circles, coloured by depth) beneath SE Asia with location of ancient Indonesian subduction trench (Getech 2012, personal communication) where thickness of line represents year. (d) Two N-S cross-sections through S40RTS tomography model in Indonesia and SE Asia subduction regions.

slab and potentially causing the proposed slab tear that separates the steeply dipping Mariana slab and the shallower dipping Izu-Bonin slab (van der Hilst *et al.* 1991; Castle & Creager 1999). However, the time period in which the trench motion changed is still debated, with suggestions of 17 Ma ago (Seno & Maruyama 1984) and 8 Ma ago (Miller *et al.* 2006). If the scatterers are indeed subducted crust in the lower mantle, we can use their presence to constrain the subduction style and temporal changes in style in the region. As we observe scatterers related to the Mariana slab down to depths of 1480 km, we can estimate the minimum time that the slab has been in the lower mantle. To travel these 820 km at 4.84 cm yr^{-1} and assuming vertical subduction in the lower mantle, the slab must have been steeply penetrating the 660 km discontinuity 16.9 Ma ago (Fig. 13), agreeing with the trench retreat and advancement model proposed by Seno & Maruyama (1984). The scatterers could be supported by the model of Miller *et al.* (2006) if subduction rates were a lot faster in the past (>10 cm yr^{-1}), but these are not reported in the literature. If we consider that the deepest scatterers found from Kaneshima & Helffrich (2009) are also part of the Mariana slab, the subducted slab must have started penetrating into the lower mantle ~26 Ma ago. Though slab penetration could have been initialized more recently if the subducted rates were significantly greater in the past.

The deep scatterers in the west of our study region trace the shape of the present-day Indonesian trench at depth. The scatterers are correlated with the locations of the palaeo-Indonesian subduction trenches between 82 and 144 Ma (Getech, 2012, personal communication). It is plausible for the slab to have entered the lower mantle by 144 Ma since it formed at 180 Ma and descended to 1880 km depth. Although the scatterers are consistent with the present-day shape of the slab in map view, a steeply dipping planar slab is not supported by the shape of the ancient subduction trenches as shown in Fig. 12(c). Geodynamic models show significant amount of buckling and thickening of subducted slabs as they travel into

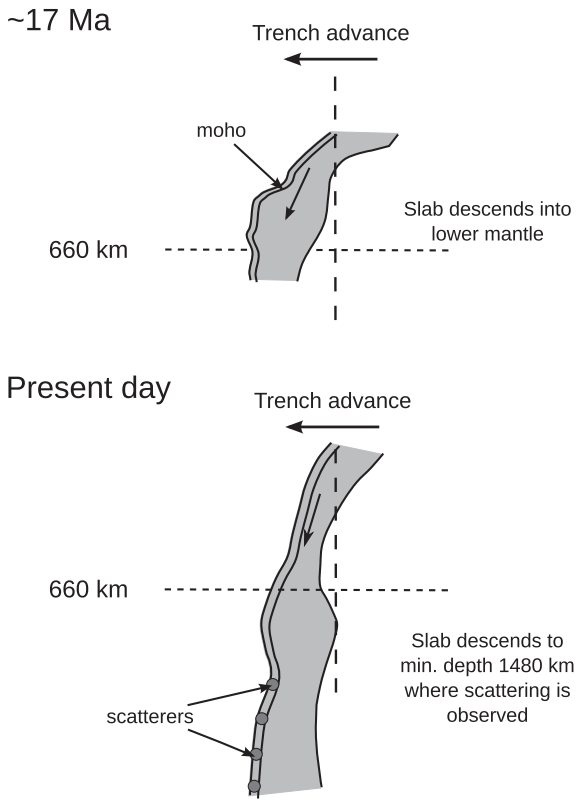

Figure 13. Schematic of the evolution of the Mariana subducted slab over last 17 Ma. The minimum depth extent of the present-day slab (bottom) can be inferred from the presence of scatterers (dark grey circles) to depths of 1480 km. After Miller *et al.* (2006).

and through the lower mantle (Lee & King 2011), though such models are generated with simple linear trench styles and do not take realistic trench geometries into account (Fig. 12). Nonetheless, the scatterers possibly image the subducted crust of this ancient slab in the lower mantle.

The method developed here is not sensitive to the whole of the Western Pacific region, including the area between the present-day Indonesian trench and the observed scatterers of the inferred deep palaeo-Indonesian slab (Fig. 8). However, tomographic images indicate that the Indonesian slab is horizontal at ∼900 km at 15°N and scattering has been previously detected at depths of 930 to 1070 km using *S*-to-*P* conversions (Vanacore *et al.* 2006). In contrast, it is possible that our method can detect scattering beneath the Philippine Sea for depths >1000 km but we do not observe any scatterers in the region (Fig. 8). The absence of scattering may suggest that slab material does not cross the 660 km discontinuity in this region. This conclusion is supported by tomographic images showing a fast anomaly at the base of the transition zone that is disconnected to other fast anomalies that have been interpreted as subducted slabs (Huang & Zhao 2006). Rost *et al.* (2008) have observed some scattering under the Philippine Sea, to depths of ∼900 km and the depth of scattering increases towards the eastern region of the Philippine Sea, close to the scatterers found in this study. It is possible that the ancient Mariana slab crossing the 660 km discontinuity has provided a preferred route for subducted slab material trapped in the transition zone (from Japan and other trenches) to descend into the lower mantle. Such a complex scenario may require subducted material to be deformed in the transition zone (Schellart 2011) and cease to be a rigid structure. We also observe scatterers to the east of Izu-Bonin and Mariana trenches. It is not clear how these would fit into the history of subduction of this region and it is possible that they are from older palaeo-subduction systems.

The detected scatterers are all located shallower than 1900 km although it is possible to detect heterogeneities at larger depths despite decreasing likelihood (Fig. 8). However, we detect far fewer scatterers in the mid- and lower mantle (deeper than 600 km) than we expect from the detection capabilities of the method, suggesting that a change in mantle heterogeneity is responsible for the decrease of scattering at these depths. The geometry of source–receiver locations and the orientation of the slab could have a strong influence on whether the scattered or reflected energy arrives at the array. Also, impedance contrasts could be a major influence as both basalt-pyrolite and basalt-harzburgite impedance contrasts sharply decrease at 1500 km depth (Rost *et al.* 2008), confirmed by the weak scattering observed in this study.

Currently, we cannot resolve whether the crust remains connected to the underlying lithosphere as it descends into the lower mantle due to the different uncertainties in tomographic and scattering imaging. Kinematic numerical modelling studies have shown that slabs are deformed greatly as the viscosity increases at the 660 km discontinuity (e.g. Stegman *et al.* 2010; Lee & King 2011) and calculations demonstrate that mechanical stirring may breakdown the crustal component throughout the mantle after 100 Ma of mixing (Stixrude & Lithgow-Bertelloni 2012). Some dynamic models show small-scale convection in the mid-mantle, which, in turn, could cause the breakdown of subducted crust leading to very small-scale (2 km) heterogeneity distributed throughout the mantle as observed through modelling global mantle heterogeneity (Earle & Shearer 2001). However, it has been suggested that the crust does not detach from the slab until it descends into the lower mantle (e.g. Christensen & Hofmann 1994; Miller & Niu 2008) and it has been shown that it is possible to accumulate crust at the base of the mantle (Christensen & Hofmann 1994).

7 CONCLUSIONS

We have found precursors to *PP* that are related to scattering at small-scale mantle heterogeneities in Western Pacific subduction zones. Using novel array methods, we have found >200 scatterers in the crust and upper mantle and 17 scatterers deeper than 600 km. In the upper mantle, scatterer locations correlate well with subducted slabs as inferred from tomography and subduction contours; thus, there is strong support that we image the heterogeneous subducted crust. Extrapolating this conclusion to deeper scatterers where the resolution of tomography is reduced, it is likely that we image the crustal component of the subducted slab in the lower mantle beneath the Izu-Bonin and Mariana trenches and beneath the location of Indonesian palaeo-subduction trench from 80 to 144 Ma. Scatterer locations are not dependent on the detection and relocation methods applied here but scatterer detections do depend on the elastic properties and the orientation of the heterogeneities.

Within this study, we demonstrate that accurate measurements can be made from a small-aperture seismic array and that these are extremely useful in revealing structures across the mantle. We have developed an automatic approach that can be used for other source–receiver paths as an objective and robust tool to detect many more mantle heterogeneities. Using a larger data set of *P*-to-*P* scattering will likely lead to a better characterization of the heterogeneities especially at larger depths and will allow linking slab dynamics with heterogeneity structure. The mantle heterogeneities we do observe

can be used to constrain geodynamic models that reveal more about the patterns of mantle mixing over geologically time.

ACKNOWLEDGEMENTS

Array data were extracted from the IRIS data holdings (www.iris.edu). Data processing was completed using Seismic Handler (Stammler 1993) and Matlab. Maps were produced using GMT (Wessel & Smith 1998). We thank Getech (http://www.getech.com) for useful discussions and for sharing subduction contours. Fenglin Niu (Rice University) provided the 1-D ray tracing code used in the relocation. This work was funded through a NERC Doctoral Training Grant.

REFERENCES

Capon, J., 1969. High-resolution frequency-wavenumber spectrum analysis, *Proc. IEEE,* **57**(8), 1408–1418.

Castle, J.C. & Creager, K.C., 1999. A steeply dipping discontinuity in the lower mantle beneath Izu-Bonin, *J. geophys. Res.,* **104**(B4), 7279–7292.

Christensen, U.R. & Hofmann, A.W., 1994. Segregation of subducted oceanic crust in the convecting mantle, *J. geophys. Res.,* **99**(B10), 19 867–19 884.

Davies, G. & Richards, M., 1992. Mantle convection, *J. Geol.,* **100**(2), 151–206.

Deschamps, F., Tackley, P.J. & Nakagawa, T., 2010. Temperature and heat flux scalings for isoviscous thermal convection in spherical geometry, *Geophys. J. Int.,* **182**(1), 137–154.

Deuss, A., Redfern, S.A.T., Chambers, K. & Woodhouse, J.H., 2006. The nature of the 660-kilometer discontinuity in Earth's mantle from global seismic observations of PP precursors, *Science,* **311**(5758), 198–201.

Dziewonski, A.M. & Woodhouse, J.H., 1987. Global images of the Earth's interior, *Science,* **236,** 37–48.

Earle, P. & Shearer, P., 2001. Distribution of fine-scale mantle heterogeneity from observations of Pdiff coda, *Bull. seism. Soc. Am.,* **91**(6), 1875–1881.

Engdahl, E.R., van der Hilst, R.D. & Berrocal, J., 1995. Imaging of subducted lithosphere beneath South America, *Geophys. Res. Lett.,* **22**(16), 2317–2320.

Engebretson, D., Kelley, K., Cashman, H. & Richards, M., 1992. 180 million years of subduction, *GSA Today,* **2**(5), 93–100.

Estabrook, C.H. & Kind, R., 1996. The nature of the 660-kilometer upper-mantle seismic discontinuity from precursors to the PP phase, *Science,* **274**(5290), 1179–1182.

Flanagan, M.P. & Shearer, P.M., 1998. Global mapping of topography on transition zone velocity discontinuities by stacking SS precursors, *J. geophys. Res.,* **103**(B2), 2673–2692.

Grand, S.P., 2002. Mantle shear-wave tomography and the fate of subducted slabs, *Phil. Trans. R. Soc. Lond., A: Math. Phys. Eng. Sci.,* **360**(1800), 2475–2491.

Gudmundsson, Ó. & Sambridge, M., 1998. A regionalized upper mantle (RUM) seismic model, *J. geophys. Res.,* **103**(B4), 7121–7136.

Hall, R., 2012. Late Jurassic/Cenozoic reconstructions of the Indonesian region and the Indian Ocean, *Tectonophysics,* **570-571,** 1–41.

Hayes, G.P., Wald, D.J. & Johnson, R.L., 2012. Slab1.0: a three-dimensional model of global subduction zone geometries, *J. geophys. Res.,* **117**(B1), B01302, doi:10.1029/2011JB008524.

Helffrich, G., 2006. Heterogeneity in the mantle; its creation, evolution and destruction, *Tectonophysics,* **416**(1–4), 23–31.

Helffrich, G.R., Stein, S. & Wood, B.J., 1989. Subduction zone thermal structure and mineralogy and their relationship to seismic wave reflections and conversions at the slab/mantle interface, *J. geophys. Res.,* **94**(B1), 753–763.

Hofmann, A.W., 1997. Mantle geochemistry: the message from oceanic volcanism, *Nature,* **385**(6613), 219–229.

Huang, J. & Zhao, D., 2006. High-resolution mantle tomography of China and surrounding regions, *J. geophys. Res.,* **111**(B9), B09305, doi:10.1029/2005JB004066.

Irifune, T. & Tsuchiya, T., 2007. *Mineralogy of the Earth - Phase Transitions and Mineralogy of the Lower Mantle,* Elsevier.

Kaneshima, S., 2009. Seismic scatterers at the shallowest lower mantle beneath subducted slabs, *Earth planet. Sci. Lett.,* **286**(1–2), 304–315.

Kaneshima, S. & Helffrich, G., 1999. Dipping low-velocity layer in the mid-lower mantle; evidence for geochemical heterogeneity, *Science,* **283**(5409), 1888–1891.

Kaneshima, S. & Helffrich, G., 2009. Lower mantle scattering profiles and fabric below Pacific subduction zones, *Earth planet. Sci. Lett.,* **282**(1), 234–239.

Kaneshima, S. & Helffrich, G., 2010. Small scale heterogeneity in the mid-lower mantle beneath the circum-Pacific area, *Phys. Earth planet. Inter.,* **183**(1–2), 91–103.

Kato, M. & Hirahara, K., 1991. Precursory arrivals to PP, *Geophys. J. Int.,* **106**(3), 551–557.

Kennett, B.L.N., Engdahl, E.R. & Buland, R., 1995. Constraints on seismic velocities in the Earth from traveltimes, *Geophys. J. Int.,* **122**(1), 108–124.

King, D.W., Haddon, R.A.W. & Husebye, E.S., 1975. Precursors to PP, *Phys. Earth planet. Inter.,* **10**(2), 103–127.

Kito, T., Thomas, C., Rietbrock, A., Garnero, E.J., Nippress, S.E.J. & Heath, A.E., 2008. Seismic evidence for a sharp lithospheric base persisting to the lowermost mantle beneath the Caribbean, *Geophys. J. Int.,* **174**(3), 1019–1028.

Krüger, F., Baumann, M., Scherbaum, F. & Weber, M., 2001. Mid-mantle scatterers near the Mariana slab detected with a double array method, *Geophys. Res. Lett.,* **28**(4), 667–670.

Lee, C. & King, S.D., 2011. Dynamic buckling of subducting slabs reconciles geological and geophysical observations, *Earth planet. Sci. Lett.,* **312**(3–4), 360–370.

Lindquist, K.G., Tibuleac, I.M. & Hansen, R.A., 2007. A semiautomatic calibration method applied to a small-aperture Alaskan seismic array, *Bull. seism. Soc. Am.,* **97**(1B), 100–113.

Miller, M.S., Kennett, B.L.N. & Toy, V.G., 2006. Spatial and temporal evolution of the subducting Pacific plate structure along the Western Pacific margin, *J. geophys. Res.,* **111**(B2), B02401, doi:10.1029/2005JB003705.

Miller, M.S. & Niu, F., 2008. Bulldozing the coreâmantle boundary: localized seismic scatterers beneath the Caribbean sea, *Phys. Earth planet. Inter.,* **170**(1–2), 89–94.

Neidell, N.S. & Tanner, M.T., 1971. Semblance and other coherency measures for multichannel data, *Geophysics,* **36**(3), 482–497.

Niu, F., Kawakatsu, H. & Fukao, Y., 2003. Seismic evidence for a chemical heterogeneity in the mid-mantle: a strong and slightly dipping seismic reflector beneath the Mariana subduction zone, *J. geophys. Res.,* **108**(B9), 2419, doi:10.1029/2002JB002384.

Obayashi, M., Yoshimitsu, J. & Fukao, Y., 2009. Tearing of stagnant slab, *Science,* **324**(5931), 1173–1175.

Patchett, P.J., White, W.M., Feldmann, H., Kielinczuk, S. & Hofmann, A., 1984. Hafnium/rare earth element fractionation in the sedimentary system and crustal recycling into the Earth's mantle, *Earth planet. Sci. Lett.,* **69**(2), 365–378.

Plank, T. & Langmuir, C.H., 1998. The chemical composition of subducting sediment and its consequences for the crust and mantle, *Chem. Geol.,* **145**(3-4), 325–394.

Quinteros, J., Sobolev, S.V. & Popov, A.A., 2010. Viscosity in transition zone and lower mantle: implications for slab penetration, *Geophys. Res. Lett.,* **37,** L09307, doi:10.1029/2010GL043140.

Ranero, C.R., Phipps Morgan, J., McIntosh, K. & Reichert, C., 2003. Bending-related faulting and mantle serpentinization at the middle America trench, *Nature,* **425**(6956), 367–373.

Rapp, R.P., Irifune, T., Shimizu, N., Nishiyama, N., Norman, M.D. & Inoue, T., 2008. Subduction recycling of continental sediments and the origin of geochemically enriched reservoirs in the deep mantle, *Earth planet. Sci. Lett.,* **271**(1–4), 14–23.

Revenaugh, J. & Jordan, T., 1991. Mantle layering from ScS reverberations. 2. The transition zone, *J. geophys. Res.,* **96**(B12), 19 763–19 780.

Richards, M. & Engebretson, D., 1992. Large-scale mantle convection and the history of subduction, *Nature,* **355**(6359), 437–440.
Ritsema, J., Deuss, A., van Heijst, H.J. & Woodhouse, J.H., 2011. S40RTS: a degree-40 shear-velocity model for the mantle from new Rayleigh wave dispersion, teleseismic traveltime and normal-mode splitting function measurements, *Geophys. J. Int.,* **184**(3), 1223–1236.
Ritsema, J., van Heijst, H.J. & Woodhouse, J.H., 1999. Complex shear wave velocity structure imaged beneath Africa and Iceland, *Science,* **286**(5446), 1925–1928.
Rost, S., Garnero, E.J. & Williams, Q., 2008. Seismic array detection of subducted oceanic crust in the lower mantle, *J. geophys. Res.,* **113,** B06303, doi:10.1029/2007JB005263.
Rost, S., Thorne, M.S. & Garnero, E.J., 2006. Imaging global seismic phase arrivals by stacking array processed Short-Period data, *Seism. Res. Lett.,* **77**(6) 697–707.
Rost, S. & Weber, M., 2001. A reflector at 200 km depth beneath the Northwest Pacific, *Geophys. J. Int.,* **147**(1), 12–28.
Rost, S. & Weber, M., 2002. The upper mantle transition zone discontinuities in the Pacific as determined by short-period array data, *Earth planet. Sci. Lett.,* **204**(3–4), 347–361.
Schellart, W.P., 2011. A subduction zone reference frame based on slab geometry and subduction partitioning of plate motion and trench migration, *Geophys. Res. Lett.,* **38**(16), L16317, doi:10.1029/2011GL048197.
Seno, T. & Maruyama, S., 1984. Paleogeographic reconstruction and origin of the Philippine Sea, *Tectonophysics,* **102**(1–4), 53–84.
Shearer, P.M., 1990. Seismic imaging of upper-mantle structure with new evidence for a 520-km discontinuity, *Nature,* **344**(6262), 121–126.
Stammler, K., 1993. Seismichandler – programmable multichannel data handler for interactive and automatic processing of seismological analyses, *Comput. Geosci.,* **19**(2), 135–140.
Stegman, D., Farrington, R., Capitanio, F. & Schellart, W., 2010. A regime diagram for subduction styles from 3-D numerical models of free subduction, *Tectonophysics,* **483**(1–2), 29–45.
Stixrude, L. & Lithgow-Bertelloni, C., 2012. Geophysics of chemical heterogeneity in the mantle, *Ann. Rev. Earth. planet. Sci.,* **40**(1), 569–595.
Tackley, P.J., 2000. Mantle convection and plate tectonics: toward an integrated physical and chemical theory, *Science,* **288**(5473), 2002–2007.
Thorne, M.S., Garnero, E.J. & Grand, S.P., 2004. Geographic correlation between hot spots and deep mantle lateral shear-wave velocity gradients, *Phys. Earth planet. Inter.,* **146**(1–2), 47–63.
van der Hilst, R. & Seno, T., 1993. Effects of relative plate motion on the deep structure and penetration depth of slabs below the Izu-Bonin and Mariana island arcs, *Earth planet. Sci. Lett.,* **120**(3–4), 395–407.
van der Hilst, R., Engdahl, E.R., Spakman, W. & Nolet, G., 1991. Tomographic imaging of subducted lithosphere below Northwest Pacific island arcs, *Nature,* **353,** 37–42.
van Keken, P.E., Hauri, E.H. & Ballentine, C.J., 2002. Mantle mixing: the generation, preservation, and destruction of chemical heterogeneity, *Ann. Rev. Earth. planet. Sci.,* **30**(1), 493–525.
Vanacore, E., Niu, F. & Kawakatsu, H., 2006. Observations of the mid-mantle discontinuity beneath Indonesia from S to P converted waveforms, *Geophys. Res. Lett.,* **33**(4), L04302, doi:10.1029/2005GL025106.
Weber, M. & Wicks, C.W., 1996. Reflections from a distant subduction zone, *Geophys. Res. Lett.,* **23**(12), 1453–1456.
Wen, L. & Anderson, D.L., 1995. The fate of slabs inferred from seismic tomography and 130 million years of subduction, *Earth planet. Sci. Lett.,* **133**(1–2), 185–198.
Wessel, P. & Smith, W.H.F., 1998. New, improved version of generic mapping tools released, *EOS, Trans. Am. geophys. Un.,* **79**(47), 579.
Widiyantoro, S., Kennett, B.L.N. & van der Hilst, R., 1999. Seismic tomography with P and S data reveals lateral variations in the rigidity of deep slabs, *Earth planet. Sci. Lett.,* **173**(1–2), 91–100.
Wright, C., 1972. Array studies of seismic waves arriving between *P* and *PP* in the distance range 90 degrees to 115 degrees, *Bull. seism. Soc. Am.,* **62**(1), 385–400.

SUPPORTING INFORMATION

Additional Supporting Information may be found in the online version of this article:

Figure S1. Selecting the Normalized Semblance Weighted Beampower (NSWB) threshold for the automatic picking of PP precursors.
Figure S2. Polar plots in slowness and backazimuth space showing vectors of theoretical and observed PP directivity, before and after the slowness correction has been applied.
Figure S3. Timing errors associated with using a 1-D reference model (ak135) for locating the scatterers.
Figure S4. Subduction contours for western Pacific subduction zones.
Table S1. Relocation cases used for error analysis of relocation procedure (http://gji.oxfordjournals.org/lookup/suppl/doi:10.1093/gji/ggu043/-/DC1).

Please note: Oxford University Press is not responsible for the content or functionality of any supporting materials supplied by the authors. Any queries (other than missing material) should be directed to the corresponding author for the article.